Editors' Suggestion

Raman Forbidden Layer-Breathing Modes in Layered Semiconductor Materials Activated by Phonon and Optical Cavity Effects

Miao-Ling Lin,[1,2] Jiang-Bin Wu,[1,2] Xue-Lu Liu,[1] Tao Liu,[1,2] Rui Mei,[1,2] Heng Wu,[1,2] Shan Guan,[1] Jia-Liang Xie,[1,2] Jun-Wei Luo,[1,2] Lin-Wang Wang,[3] Andrea C. Ferrari,[4] and Ping-Heng Tan[1,2,*]

[1]*State Key Laboratory of Semiconductor Physics and Chip Technologies, Institute of Semiconductors, Chinese Academy of Sciences, Beijing 100083, China*

[2]*Center of Materials Science and Optoelectronics Engineering, University of Chinese Academy of Sciences, Beijing 100049, China*

[3]*State Key Laboratory of Optoelectronic Materials and Devices, Institute of Semiconductors, Chinese Academy of Sciences, Beijing 100083, China*

[4]*Cambridge Graphene Centre, University of Cambridge, 9 JJ Thomson Avenue, Cambridge CB3 0FA, United Kingdom*

(Received 21 September 2024; revised 13 December 2024; accepted 13 January 2025; published 7 March 2025)

We report Raman forbidden layer-breathing modes (LBMs) in layered semiconductor materials (LSMs). The intensity distribution of all observed LBMs depends on layer number, incident light wavelength, and refractive index mismatch between LSM and underlying substrate. These results are understood by a Raman scattering theory via the proposed spatial interference model, where the naturally occurring optical and phonon cavities in LSMs enable spatially coherent photon-phonon coupling mediated by the corresponding one-dimensional periodic electronic states. Our work reveals the impact of spatial coherence of photon and phonon fields on phonon excitation via photon or phonon cavity engineering.

DOI: 10.1103/PhysRevLett.134.096903

Raman scattering is a ubiquitous tool for probing elementary excitations [1–3] (e.g., phonons) and electron (exciton)-photon or -phonon (*e*-pht and *e*-phn, respectively) interactions [4–6] in both bulk and nanoscale materials. In the quantum picture of Raman scattering, incident photons first excite a set of intermediate electronic states, which then generate or absorb phonons and give rise to energy-shifted scattered photons [1,7]. The intermediate electronic excitations are pivotal as quantum pathways in Raman scattering [7–9] and determine the *e*-pht and *e*-phn interaction matrix elements [1,4,6,10]. Traditionally, these can be evaluated by making a multipole expansion [1], based on the premise that the wavelength of light is large compared with atomic dimensions. Usually, only the first term of the multipole expansion, i.e., electric dipole, is retained [1], defining the Raman tensor based on group symmetry analysis to determine the polarization selection rules [1,11]. An interlayer bond polarizability model (IBPM) within this approximation was also developed to understand the Raman intensity of interlayer phonons in ultrathin layered materials (LMs) [12,13] and in LM heterostructures showing cross-dimensional *e*-phn coupling [14]. In this case, the *e*-pht matrix element is considered independent of the photon wave vector.

If incident light wavelength and dimension of phonon displacement field are comparable, the premise for multipole expansion fails, leading to the breakdown of the Raman selection rules based on symmetry analysis. It is a challenge to achieve matching between light wavelength and dimension of phonon displacement fields for Raman scattering in bulk solids. However, LMs can act as phonon cavity [15–17] by generating standing waves, enabling wavelength (and wave vector) matching between photon field and the phonon field standing waves by adjusting LM thickness and dielectric environment. LMs can also generate a Fabry-Pérot optical cavity with photon field redistribution for enhanced light-matter interaction [18,19], which could induce a change in photon-phonon (pht-phn) coupling. These cavity effects could result in new Raman selection rules.

Here, we show that layered semiconductor materials (LSMs) with specific thicknesses can act as a naturally occurring optical cavities and induce spatial variations in the photon field inside LSMs, and a phonon cavity to match the photon wave vector with quantized standing-wave vectors of layer-breathing phonons along the out-of-plane axis. The two effects result in spatially modulated *e*-pht and *e*-phn interactions and the observation of Raman forbidden layer-breathing modes (LBMs). A spatial interference model (SIM) of pht-phn coupling that integrates *e*-pht and *e*-phn interactions is presented to describe the intensity of Raman-inactive LBMs dependent on LBM standing-wave vectors, LSM layer number, excitation wavelength, and the underlying substrate. This novel Raman scattering theory of pht-phn coupling goes beyond the traditional electric dipole approximation in Raman tensor theory.

*Contact author: phtan@semi.ac.cn

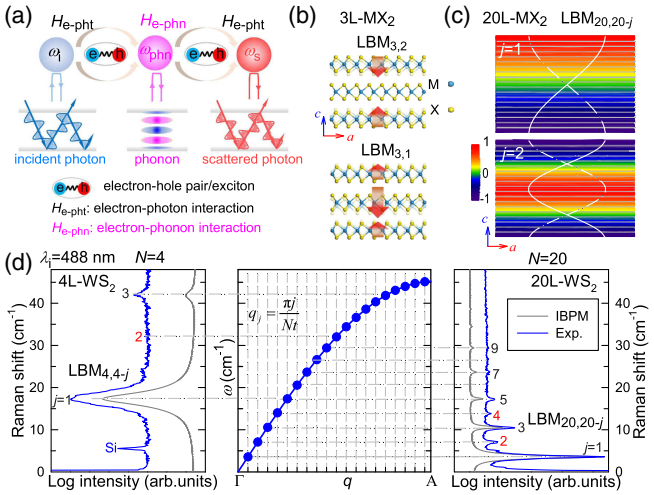

FIG. 1. (a) Raman scattering modulated by photon or phonon fields overlapping in a cavity. (b) Displacements of LBMs in 3L-MX_2, where the arrow length represents the vibration amplitude. (c) Side view of displacement field profiles of $\mathrm{LBM}_{20,20-j}$ ($j = 1,2$) in 20L-MX_2, where the color represents the amplitude. (d) $\omega - q$ along $\Gamma - A$ direction with q-dependent $\mathrm{Pos}(\mathrm{LBM}_{N,N-j})$ in 4L- and 20L-WS_2 and experimental (blue) and IBPM predicted (gray) Raman spectra of the corresponding LBMs.

We consider the interaction diagram in a Raman scattering event involving one phonon excitation [Fig. 1(a)], where ω_i, ω_s, and ω_phn are the frequencies of incident (i), scattered (s) photons, and phonon, respectively. The interactions between incident or scattered photons and phonons are mediated by electron-hole (e-h) pairs [1] or excitons [20], where e-pht and e-phn interactions are characterized by the corresponding matrix elements $M_{e\text{-pht(i/s)}}$ and $M_{e\text{-phn}}$ [1]. The output in this scattering event is determined by a third-order perturbation process [1,21]:

$$I \propto \left| \sum_{e,e'} \frac{M_{e\text{-pht(i)}} M_{e\text{-phn}} M_{e\text{-pht(s)}}}{(\hbar\omega_\mathrm{i} - \epsilon_{e\text{-h}} + i\gamma)(\hbar\omega_\mathrm{s} - \epsilon_{e'\text{-h}} + i\gamma)} \right|^2, \quad (1)$$

where h, e and e' label the states of the photoexcited hole, photoexcited electron and scattered electron, respectively, $\omega_\mathrm{s} = \omega_\mathrm{i} \pm \omega_\mathrm{phn}$, $\epsilon_{e\text{-h}}$ and $\epsilon_{e'\text{-h}}$ are the energies of electronic transitions, and γ is the homogeneous linewidth of the electronic transition [1,21]. The Raman intensity is sensitive to the pht-phn coupling, i.e., $M_{e\text{-pht(i)}} M_{e\text{-phn}} M_{e\text{-pht(s)}}$, and the detuning of the involved photon from inherent optical resonances [1,7,10,22–24]. Once incident or scattered photon and phonon are confined and overlap in a cavity, both $M_{e\text{-pht}}$ and $M_{e\text{-phn}}$ can exhibit spatial variations within the cavity, resulting in constructive or destructive interference of pht-phn coupling in real space.

Here we use LSM flakes with layer number $N > 1$, such as MX_2 (M = Mo, W and X = S, Se) (NL-MX_2). These have $N-1$ phonon modes involving the relative motions of atomic planes along the out-of-plane (c) axis, i.e., $\mathrm{LBM}_{N,N-j}$ ($j = 1, 2 \ldots N-1$) [22,25–28], as depicted by LBM_{3-j} ($j = 1, 2$) of 3L-MX_2 in Fig. 1(b). According to the linear chain model [25–28], the atomic plane displacements are given by $u_\mathrm{LBM}(q_j, z) = (e^{iq_j z} + e^{-iq_j z})/2$, where $q_j = \pi j/(Nt) = j\delta q$ ($j = 1, 2 \ldots N-1$) with δq being the q_j difference between two adjacent LBMs and $z = (2n-1)t/2$ with n the layer index and t the thickness of monolayer. Thus, LBMs can be considered as phonon cavity modes showing standing-wave feature with wavelength $\lambda_{\mathrm{LBM}_{N,N-j}} = 2Nt/j$, i.e., the superposition of two one-dimensional (1d) counterpropagating plane-wave components (out-of-plane), labeled $+q_j$ ($-q_j$) for the components propagating away from (toward) the sample surface, as exemplified by the displacement field profiles of $\mathrm{LBM}_{20,20-j}$ ($j = 1, 2$) for 20L-MX_2 [color contour and white curves in Fig. 1(c)]. The quantized q_j along the c axis corresponds to the standing-wave vector of LBM displacement fields in LSMs. This phonon cavity characteristic for LBMs in LSMs provides a platform to enable wave vector matching between a photon and the standing wave of phonons by tuning N. The frequencies of the $N-1$ LBMs are also dependent on q_j and can be derived from the linear chain model [25–28] as $\mathrm{Pos}(\mathrm{LBM}_{N,N-j}) = \mathrm{Pos}(\mathrm{LBM}_\infty) \sin(q_j t/2)$, where $\mathrm{Pos}(\mathrm{LBM}_\infty)$ represents the peak position of the LBM in a bulk LSM. $\mathrm{Pos}(\mathrm{LBM}_{N,N-j})$ can be also expressed by the dispersion $\omega - q$ of the longitudinal acoustic phonons in bulk MX_2 along $\Gamma - A$ direction [$q_\mathrm{A} = (0, 0, \pi/t)$] [29], in which the confinement of NL-MX_2 in the c axis limits q_j of $\mathrm{LBM}_{N,N-j}$ to integral multiples of π/Nt, as demonstrated for 4L- and 20L-WS_2 in Fig. 1(d).

To probe the LBMs in WS_2 flakes, we use an incident photon energy of 2.54 eV (Sec. I and Fig. S1 in Supplemental Material [30]), resonant with the C exciton energy ~2.6 eV [42,43]. The experimental $\mathrm{LBM}_{N,N-j}$ intensity distribution of 4L-WS_2 [Fig. 1(d)] can be understood by the IBPM (Sec. II in Supplemental Material [30]), with $\mathrm{LBM}_{N,N-j}$ (j is odd) peaks and absence of even $\mathrm{LBM}_{N,N-j}$ (j is even; Fig. S2 in Supplemental Material [30]). However, for 20L-WS_2, significant differences emerge, particularly with the rising intensity of even $\mathrm{LBM}_{N,N-j}$ peaks, predicted to be Raman-inactive by the IBPM [Fig. 1(d)] and symmetry analysis. 20L-WS_2 exhibits much smaller q_j (0.25 nm^{-1} when $j = 1$) than that (1.27 nm^{-1} when $j = 1$) in 4L-WS_2. The former is comparable with the change of the light wave vector ($\Delta k = 2k_\mathrm{i} = 0.13$ nm^{-1}, where $k_\mathrm{i} = 2\pi\tilde{n}_1/\lambda_\mathrm{i}$ is the wave vector at incident laser wavelength λ_i within a LSM with refractive index $\tilde{n}_1$) in backscattering configuration. This suggests a novel mechanism ruling the observation of forbidden even $\mathrm{LBM}_{N,N-j}$, due to the wave vector matching between an incident or scattered photon and standing wave of LBM phonon within a 20L-WS_2 cavity.

For specific $\hbar\omega_{\rm i}$ (or $\lambda_{\rm i}$), the Raman intensity of LBMs in LSMs is usually determined by $M_{e\text{-pht(i)}}M_{e\text{-phn}}M_{e\text{-pht(s)}}$ in Eq. (1). We first consider the e-phn interaction term $M_{e\text{-phn}}$. $\hbar\omega_{\rm i} = 2.54$ eV can resonantly excite e-h pairs close to Γ point of Brillouin zone related to the C exciton of WS_2 flakes, confined within each layer [44] (Sec. III and Fig. S3 in Supplemental Material [30]) and form an ensemble of confined electronic states (i.e., 1d periodic electronic states [44,45]). The standing-wave nature of LBMs generates a lattice dilation along the c axis. Thus, $M_{e\text{-phn}}$ between delocalized LBMs and the 1d periodic electronic states can be expressed by the deformation-potential interaction [21,31] as (Sec. III in Supplemental Material [30]):

$$M_{e\text{-phn}} \propto \frac{\frac{1}{2} \pm \frac{1}{2} + n(q_j)}{\omega_{\rm phn}} \int |\Psi(z)|^2 m_{\rm ph}(q_j z) dz, \quad (2)$$

where $\Psi(z)$ is the 1d periodic electronic wave function, $m_{\rm ph}(q_j, z) = e^{iq_j z} - e^{-iq_j z}$ gives the lattice dilation along the c axis, $n(q_j)$ is the Bose-Einstein population factor, and the $+(-)$ sign stands for Stokes (anti-Stokes) Raman scattering. The layer displacements of LBMs lead to significant spatial modulation of $M_{e\text{-phn}}$, which depends on q_j. Within the electric dipole approximation, $M_{e\text{-pht(i/s)}}$ is considered as constant with polarization direction of the incident (scattered) light. In this case, the LBM intensity is proportional to $|M_{e\text{-phn}}|^2$. The corresponding calculated LBM spectrum (Fig. S4 in Supplemental Material [30]) does not have even LBMs for 20L-WS_2, in agreement with the IBPM, but in contrast with experiments. This suggests that we need to go beyond the electric dipole approximation for the e-pht coupling term $M_{e\text{-pht(i/s)}}$.

We now consider the detailed incident or scattered photon propagation in the air/LSM/substrate dielectric multilayers for Raman scattering of LBMs. The refractive index mismatch [$\Delta_{\tilde{n}} = (\tilde{n}_\mu - \tilde{n}_\nu)/(\tilde{n}_\mu + \tilde{n}_\nu)$, with $\tilde{n}_\mu$ and $\tilde{n}_\nu$ the complex refractive indexes of the adjacent media] between LSM, air, and substrate can lead to partial reflection of light at the air/LSM and LSM/substrate interfaces, resulting in an optical cavity effect. This leads to a considerable spatial modulation in the modulus square of the electric field for the incident laser inside LSMs with thickness up to 150L, as shown in Fig. 2(a), due to the superposition of forward (down) and backward (up) propagating optical waves (whose electric field components are denoted as $E_{\rm i}^{\rm D}$ and $E_{\rm i}^{\rm U}$, respectively), as shown in Fig. 2(b). The scattered optical wave generated by the recombination of scattered e-h pairs by LBMs also has two components propagating toward (up) and away from (down) the air/LSM interface, i.e., $E_{\rm s}^{\rm U}$ and $E_{\rm s}^{\rm D}$. The combination of incident and scattered electric field components can lead to two internal scattering

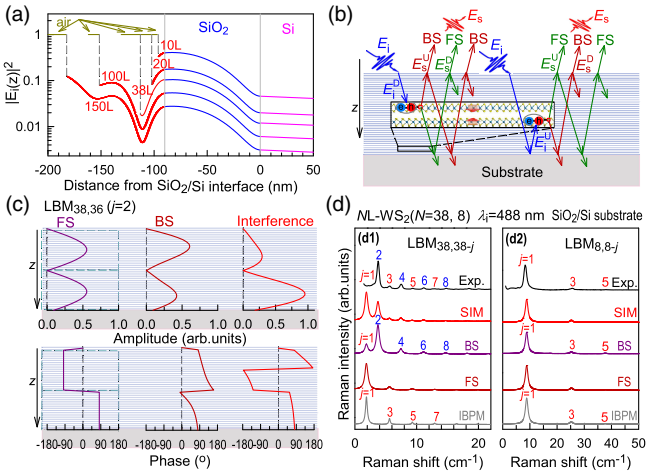

FIG. 2. (a) $|E_i(z)|^2$ in NL-WS_2/SiO_2/Si. (b) Propagation path of incident (blue) and scattered (red) photons in MX_2 flakes. Two pathways of incident and scattered photons, toward (up, U) and away from (down, D) the top surface of MX_2, result in internal FS and BS geometries. (c) Spatial variation of amplitude and phase of FS, BS, and FS-BS interfering pht-phn coupling matrixes for $LBM_{38,36}$ of 38L-WS_2. (d) LBM spectra of (d1) 38L-WS_2 and (d2) 8L-WS_2 on SiO_2/Si for FS and BS components and FS-BS interference calculated by SIM, along with IBPM-simulated and experimental (exp.) spectra.

geometries within LSM flakes, i.e., forward (FS) and backward scattering (BS). Accordingly, the e-pht coupling $[m_{e\text{-pht(i)}}(z)m_{e\text{-pht(s)}}(z)]$ at position z is derived by the product of incident and scattered electric field components (Sec. IV in Supplemental Material [30]):

$$\begin{aligned} m_{e\text{-pht(i)}}(z)m_{e\text{-pht(s)}}(z) &\propto (E_{\rm i}^{\rm U} + E_{\rm i}^{\rm D})(E_{\rm s}^{\rm U} + E_{\rm s}^{\rm D}) \\ &= t_{01}t_{10}\frac{2r_{12}e^{2ik_{\rm i}Nt} + [e^{2ik_{\rm i}z} + r_{12}^2 e^{2ik_{\rm i}(2Nt-z)}]}{(1 - r_{12}r_{10}e^{2ik_{\rm i}Nt})^2} \\ &= m_{e\text{-pht}}^{\rm FS}(2k_{\rm i}) + m_{e\text{-pht}}^{\rm BS}(2k_{\rm i}z) \end{aligned} \quad (3)$$

with $t_{\mu\nu}$ and $r_{\mu\nu}$ the amplitude transmission and reflection coefficients from medium μ to ν, respectively, and $m_{e\text{-pht}}^{\rm FS}(2k_{\rm i})$ and $m_{e\text{-pht}}^{\rm BS}(2k_{\rm i}z)$ representing the e-pht coupling of the FS and BS components.

The spatial distribution of pht-phn coupling along the c axis, including e-pht and e-phn interactions mediated by the electronic states, can be written as $[m_{e\text{-pht}}^{\rm FS}(2k_{\rm i}) + m_{e\text{-pht}}^{\rm BS}(2k_{\rm i}z)]m_{e\text{-phn}}(q_j z)$ (Sec. V in Supplemental Material [30]). Because of the localization of electronic states within the layer, a coherent summation of spatially modulated pht-phn coupling for the whole LSM leads to a variation of Raman intensity (I) as a function of q_j [or $\mathrm{Pos}(\mathrm{LBM}_{N,N-j})$]:

$$I(q_j)\sim\left|\sum_{n=0}^{N-1}[m_{e\text{-pht}}^{\mathrm{FS}}(2k_{\mathrm{i}})+m_{e\text{-pht}}^{\mathrm{BS}}(2k_{\mathrm{i}}n)]m_{e\text{-phn}}(q_jn)\right|^2$$
$$=\left|\sum_{n=0}^{N-1}\{S_{\mathrm{FS}}(2k_{\mathrm{i}},q_jn)+S_{\mathrm{BS}}[(2k_{\mathrm{i}}\pm q_j)n]\}\right|^2, \quad (4)$$

where the $S_{\mathrm{FS}}(2k_{\mathrm{i}},q_jn)$ ($S_{\mathrm{BS}}[(2k_{\mathrm{i}}\pm q_j)n]$) is the pht-phn coupling of the FS (BS) component in the nth LSM layer. We denote the above model described by Eq. (4) as SIM, this shows how the spatially coherent pht-phn coupling in the phonon and optical cavities of LSMs determines the Raman intensity of the corresponding LBMs.

We first analyze the LBM intensity distribution of thick LSMs (e.g., 38L-WS_2) based on SIM using the corresponding complex refractive indices: $5.2+1.1\mathrm{i}$ [32] for WS_2, 1.4629 [33] for SiO_2, and $4.3606+0.0868\mathrm{i}$ [33] for Si. The calculated spatial variations in amplitude and phase of $S_{\mathrm{FS/BS}}$ along the c axis for $\mathrm{LBM}_{38,36}$ ($j=2$) of 38L-WS_2 on SiO_2/Si are depicted in Fig. 2(c). The amplitude and phase of S_{FS} synchronously oscillate in real space related to q_j (Sec. V in Supplemental Material [30]). For even j (e.g., $\mathrm{LBM}_{38,36}$, $j=2$), the phase varies alternately between positive and negative values, with a shift of π (Figs. 2(c) and Fig. S5 in Supplemental Material [30]). A coherent summation of $S_{\mathrm{FS}}(2k_{\mathrm{i}},q_jn)$ for the whole LSM could result in zero intensity for even LBMs, due to spatially destructive interference (Fig. S5 in Supplemental Material [30]), and finite Raman intensity for odd LBMs, because of incompletely destructive interference (Fig. S6 in Supplemental Material [30]). Conversely, the amplitude and phase of S_{BS} are a function of $2k_{\mathrm{i}}\pm q_j$, and the phase does not always vary alternately between positive and negative values (Fig. 2(c) and Figs. S5 and S6 in Supplemental Material [30]). Thus, a coherent summation of $S_{\mathrm{BS}}[(2k_{\mathrm{i}}\pm q_j)n]$ for the whole LSM leads to the LBM intensity varying with the difference between $2k_{\mathrm{i}}$ and q_j, where the even LBM intensity is not always zero. By considering the general Lorentzian line shape of LBMs and the weighted intensity, we calculate the LBM Raman spectra from FS and BS components and FS-BS interference [Fig. 2(d1)]. When just considering the FS component, $I(q_j)$ exhibits a series of zeros at even j, leading to the observation of only odd LBMs, aligning with the IBPM predictions. However, if one considers just the BS component, even LBMs can display significantly higher intensities than the adjacent odd ones. The interference of FS and BS components leads to the excitation of both odd and even LBMs in the Raman spectrum, and the corresponding calculated LBM spectrum agrees with the experimental one [Fig. 2(d1)].

For thin LSMs, e.g., WS_2 flakes with small N (e.g., $N<10$), the condition $2k_{\mathrm{i}}\ll\Delta q$, i.e., $|q_j|\sim|2k_{\mathrm{i}}\pm q_j|$, leads to S_{BS} being close to S_{FS}. This similarity results in that the spatial amplitude and phase of the FS-BS interference closely approximate those of S_{FS}. Therefore,

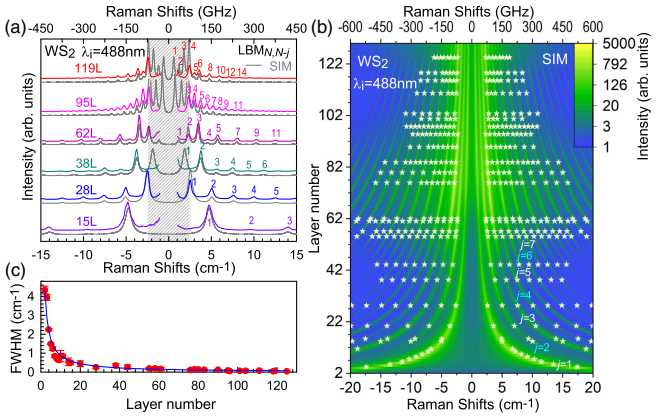

FIG. 3. (a) SIM-calculated (gray) and experimental (colored) LBM spectra. The stripe-pattered shade is the blind spectral range of our Raman setup. (b) SIM-calculated phonon spectra in NL-WS_2 ($N=2$–130). Stars are experimental data. (c) $1/N$-dependent average FWHM, where 0.16 cm^{-1} is subtracted from FWHM to account for the system broadening.

Raman spectra from FS-BS interference and BS component are similar to that of the FS component, such as the case of 8L-WS_2 in Fig. 2(d2). As N increases, the mismatch between q_j and $2k_{\mathrm{i}}\pm q_j$ enlarges, and the conditions for destructive interference cease to hold, allowing the even modes to emerge, as discussed above for 38L-WS_2.

To clearly reveal the evolution of the LBM emission with varying LSM thickness, we measure LBM spectra [Figs. 3(a) and 3(b)] of NL-WS_2 flakes on SiO_2/Si with N varying from 2 to 130 under resonant excitation of the C exciton. The calculated LBM spectra concur with the experimental results. The intensities of even LBMs relative to that of adjacent odd LBMs are significantly enhanced in specific N ranges, as demonstrated in Fig. 3(b). E.g., with $N=10$–30, the observed odd $\mathrm{LBM}_{N,N-j}$ branches exhibit stronger intensities than the adjacent even $\mathrm{LBM}_{N,N-j-1}$ branches, whereas for $N=30$–60, the intensities of the even $\mathrm{LBM}_{N,N-j}$ branches surpass those of adjacent odd $\mathrm{LBM}_{N,N-j-1}$ ones.

Figures 3(a) and 3(b) demonstrate that the frequency difference between adjacent LBMs of NL-WS_2 decreases as N increases. The average full width at half maximum (FWHM) of the LBMs also decreases with increasing N, showing a $1/N$ dependence [Fig. 3(c), blue line]. This can be ascribed to the q_j confinement of standing-wave LBMs along the c axis. The q uncertainty [Δq] can be estimated by the Heisenberg uncertainty principle, i.e., $\Delta x\Delta p\sim\hbar/2$, where $\Delta x=Nt$ and $\Delta p=\hbar\Delta q$. According to the $\mathrm{Pos(LBM)}-q_j$ relation, $\mathrm{FWHM(LBM)}\propto(t/2)\cos(q_jt/2)\times\Delta q\propto 1/N$.

SIM also implies that the intensity distribution of all the observed LBMs is sensitive to the optical cavity effect, which should be significantly dependent on the refractive index mismatch between LSM and underlying substrates. As a check, we measure the Raman spectra [Fig. 4(a)]

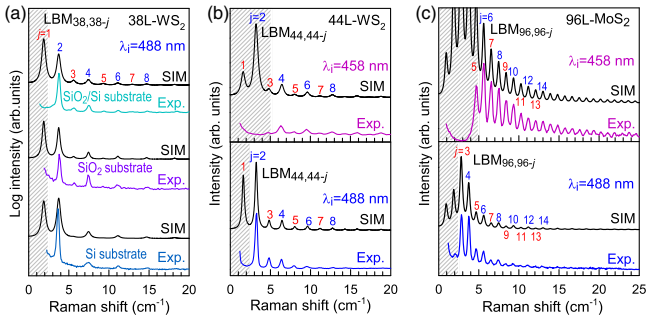

FIG. 4. (a) Experimental (exp., colored) and SIM-calculated (black) LBM spectra of 38L-WS_2 on different substrates, $\lambda_i = 488$ nm, and those for (b) 44L-WS_2 and (c) 96L-MoS_2 with $\lambda_i = 458$ nm and 488 nm.

of 38L-WS_2 on 90 nm-SiO_2/Si, bare SiO_2, and Si. A significant refractive index mismatch ($\Delta\tilde{n} \approx 0.57 + 0.07i$) between WS_2 and SiO_2 enhances the optical cavity effect, boosting the FS component [odd LBMs; Figs. 2(b) and 2(d1)] contributions to LBM spectra on 90 nm-SiO_2/Si and bare SiO_2. However, when 38L-WS_2 flakes are deposited on Si, due to the close refractive indexes of WS_2 and Si, the optical cavity effect at the 38L-WS_2/Si interface is weak, and the FS component contribution is small. Thus, odd LBMs are absent in the corresponding Raman spectrum with dominant even LBMs. The measured LBM spectra for 38L-WS_2 on different substrates agree with the SIM predictions. These results demonstrate the possibility to tune LBM emissions by varying the refractive index mismatch between LSM and underlying substrate.

Because of the importance of wave vector matching between the photon and standing wave of phonons in ruling the LBM Raman intensity, it is expected that the LBM emission will be sensitive to λ_i. Figure 4(b) presents the experimental and calculated Raman spectra of LBMs in 44L-WS_2 excited at 488 nm and 458 nm, under resonant excitation of the C exciton [43]. The different k_i lead to varying mismatches between q_j and $2k_i \pm q_j$, resulting in distinctly different interference effects at these λ_i. Compared to $\lambda_i = 488$ nm, the intensities of odd LBMs are weaker than those of adjacent even LBMs under $\lambda_i = 458$ nm in 44L-WS_2. Similar λ_i-dependent LBM spectra can be observed in other LSMs, such as MoS_2, $MoSe_2$, and $MoTe_2$, as illustrated in Figs. 4(c) and Fig. S7 (Sec. VI in Supplemental Material [30]). This supports the general applicability of the SIM, which accounts for the spatially coherent pht-phn coupling for LBMs in LSM cavities.

In conclusion, we reported the observation of forbidden LBM emission in LSMs, driven by spatially coherent coupling of the photon field propagating along the c axis and the phonon field to 1d periodic electronic states, which can be well understood by a Raman scattering theory via the proposed SIM. The Raman intensity distribution of all the observed LBMs can be tuned by varying the wave vector matching between photons and standing wave of phonons with LSM thickness, excitation wavelength, and refractive index mismatch between LSM and underlying substrate.

Acknowledgments—We acknowledge the support from the National Key Research and Development Program of China (Grant No. 2023YFA1407000), the Strategic Priority Research Program of Chinese Academy of Sciences (CAS) (Grant No. XDB0460000), National Natural Science Foundation of China (Grants No. 12322401, No. 12127807, and No. 12393832), CAS Key Research Program of Frontier Sciences (Grant No. ZDBS-LY-SLH004), Beijing Nova Program (Grant No. 20230484301), Youth Innovation Promotion Association, Chinese Academy of Sciences (No. 2023125), Science Foundation of the Chinese Academy of Sciences (Grant No. JCPYJJ-22) CAS Project for Young Scientists in Basic Research (YSBR-026), EU Graphene and Quantum Flagships, ERC Grants Hetero2D and GIPT, EU Grants GRAP-X and CHARM, and EPSRC Grants No. EP/K01711X/1, No. EP/K017144/1, No. EP/N010345/1, No. EP/L016087/1, No. EP/V000055/1, and No. EP/X015742/1.

Data availability—The data that support the findings of this Letter are openly available in the Research Gate data repository [48].

[1] *Light Scattering in Solids I*, edited by M. Cardona (Springer-Verlag, Berlin, 1983), Vol. 8.
[2] A. C. Gadelha *et al.*, Localization of lattice dynamics in low-angle twisted bilayer graphene, Nature (London) **590**, 405 (2021).
[3] S. Li, E. Drueke, Z. Porter, W. Jin, Z. Lu, D. Smirnov, R. Merlin, S. D. Wilson, K. Sun, and L. Zhao, Symmetry-resolved two-magnon excitations in a strong spin-orbit-coupled bilayer antiferromagnet, Phys. Rev. Lett. **125**, 087202 (2020).
[4] G. S. N. Eliel *et al.*, Intralayer and interlayer electron–phonon interactions in twisted graphene heterostructures, Nat. Commun. **9**, 1221 (2018).
[5] S. Zhang, J. Huang, Y. Yu, S. Wang, T. Yang, Z. Zhang, L. Tong, and J. Zhang, Quantum interference directed chiral Raman scattering in two-dimensional enantiomers, Nat. Commun. **13**, 1254 (2022).
[6] Q.-H. Tan *et al.*, Quantum interference between darkexcitons and zone-edged acoustic phonons in few-layer WS_2, Nat. Commun. **14**, 88 (2023).
[7] C.-F. Chen *et al.*, Controlling inelastic light scattering quantum pathways in graphene, Nature **471**, 617 (2011).
[8] Q. Lin, J. Rosenberg, D. Chang, R. Camacho, M. Eichenfield, K. J. Vahala, and O. Painter, Coherent mixing of mechanical excitations in nano-optomechanical structures, Nat. Photonics **4**, 236 (2010).
[9] H. P. C. Miranda, S. Reichardt, G. Froehlicher, A. Molina-Sánchez, S. Berciaud, and L. Wirtz, Quantum interference effects in resonant Raman spectroscopy of single- and triple-layer $MoTe_2$ from first-principles, Nano Lett. **17**, 2381 (2017).

[10] B. R. Carvalho, L. M. Malard, J. M. Alves, C. Fantini, and M. A. Pimenta, Symmetry-dependent exciton-phonon coupling in 2D and bulk MoS_2 observed by resonance Raman scattering, Phys. Rev. Lett. **114**, 136403 (2015).
[11] R. Loudon, The Raman effect in crystals, Adv. Phys. **13**, 423 (1964).
[12] X. Luo, X. Lu, C. Cong, T. Yu, Q. Xiong, and S. Y. Quek, Stacking sequence determines Raman intensities of observed interlayer shear modes in 2D layered materials–a general bond polarizability model, Sci. Rep. **5**, 14565 (2015).
[13] L. Liang, A. A. Puretzky, B. G. Sumpter, and V. Meunier, Interlayer bond polarizability model for stacking-dependent low-frequency Raman scattering in layered materials, Nanoscale **9**, 15340 (2017).
[14] M.-L. Lin, Y. Zhou, J.-B. Wu, X. Cong, X.-L. Liu, J. Zhang, H. Li, W. Yao, and P.-H. Tan, Cross-dimensional electron-phonon coupling in van der Waals heterostructures, Nat. Commun. **10**, 2419 (2019).
[15] M. K. Zalalutdinov *et al.*, Acoustic cavities in 2D heterostructures, Nat. Commun. **12**, 3267 (2021).
[16] S. Ge, X. Liu, X. Qiao, Q. Wang, Z. Xu, J. Qiu, P.-H. Tan, J. Zhao, and D. Sun, Coherent longitudinal acoustic phonon approaching THz frequency in multilayer molybdenum disulphide, Sci. Rep. **4**, 5722 (2014).
[17] P. Soubelet, A. A. Reynoso, A. Fainstein, K. Nogajewski, M. Potemski, C. Faugeras, and A. E. Bruchhausen, The lifetime of interlayer breathing modes of few-layer 2H-$MoSe_2$ membranes, Nanoscale **11**, 10446 (2019).
[18] X. Xu, C. Trovatello, F. Mooshammer, Y. Shao, S. Zhang, K. Yao, D. N. Basov, G. Cerullo, and P. J. Schuck, Towards compact phase-matched and waveguided nonlinear optics in atomically layered semiconductors, Nat. Photonics **16**, 698 (2022).
[19] H. Zhang, Z. Ni, C. E. Stevens, A. Bai, F. Peiris, J. R. Hendrickson, L. Wu, and D. Jariwala, Cavity-enhanced linear dichroism in a van der Waals antiferromagnet, Nat. Photonics **16**, 311 (2022).
[20] S. Reichardt and L. Wirtz, Nonadiabatic exciton-phonon coupling in Raman spectroscopy of layered materials, Sci. Adv. **6**, eabb5915 (2020).
[21] A. Mlayah, J.-R. Huntzinger, and N. Large, Raman-brillouin light scattering in low-dimensional systems: Photoelastic model versus quantum model, Phys. Rev. B **75**, 245303 (2007).
[22] A. C. Ferrari and D. M. Basko, Raman spectroscopy as a versatile tool for studying the properties of graphene, Nat. Nanotechnol. **8**, 235 (2013).
[23] E. del Corro, H. Terrones, A. Elias, C. Fantini, S. Feng, M. A. Nguyen, T. E. Mallouk, M. Terrones, and M. A. Pimenta, Excited excitonic states in 1L, 2L, 3L, and bulk WSe_2 observed by resonant Raman spectroscopy, ACS Nano **8**, 9629 (2014).
[24] K. Kim, J.-U. Lee, D. Nam, and H. Cheong, Davydov splitting and excitonic resonance effects in Raman spectra of few-layer $MoSe_2$, ACS Nano **10**, 8113 (2016).
[25] P. H. Tan *et al.*, The shear mode of multilayer graphene, Nat. Mater. **11**, 294 (2012).
[26] X. Zhang, W. P. Han, J. B. Wu, S. Milana, Y. Lu, Q. Q. Li, A. C. Ferrari, and P. H. Tan, Raman spectroscopy of shear and layer breathing modes in multilayer MoS_2, Phys. Rev. B **87**, 115413 (2013).
[27] Y. Zhao, X. Luo, H. Li, J. Zhang, P. T. Araujo, C. K. Gan, J. Wu, H. Zhang, S. Y. Quek, M. S. Dresselhaus, and Q. Xiong, Interlayer breathing and shear modes in few-trilayer MoS_2 and WSe_2, Nano Lett. **13**, 1007 (2013).
[28] G. Pizzi, S. Milana, A. C. Ferrari, N. Marzari, and M. Gibertini, Shear and breathing modes of layered materials, ACS Nano **15**, 12509 (2021).
[29] L. Karssemeijer and A. Fasolino, Phonons of graphene and graphitic materials derived from the empirical potential LCBOPII, Surf. Sci. **605**, 1611 (2011).
[30] See Supplemental Material at http://link.aps.org/supplemental/10.1103/PhysRevLett.134.096903 for details on methods, interlayer bond polarizability model for LBM in *N*L-WS_2, localized electronic states in *N*L-WS_2, optical cavity effects in LSMs, spatial interference model of photon-phonon coupling, and tunable LBM spectra in $MoSe_2$ and $MoTe_2$, which includes Refs. [12,13,21,28,31,34–44,46,47].
[31] C. Kittel *et al.*, *Introduction to Solid State Physics* (Wiley, New York, 1976), Vol. 8.
[32] Y. Li, A. Chernikov, X. Zhang, A. Rigosi, H. M. Hill, A. M. van der Zande, D. A. Chenet, E.-M. Shih, J. Hone, and T. F. Heinz, Measurement of the optical dielectric function of monolayer transition-metal dichalcogenides: MoS_2, $MoSe_2$, WS_2, and WSe_2, Phys. Rev. B **90**, 205422 (2014).
[33] *Handbook of Optical Constants of Solids*, edited by E. D. Palik (Academic Press, Burlington, 2002).
[34] S.-Y. Chen, C. Zheng, M. S. Fuhrer, and J. Yan, Helicity-resolved Raman scattering of MoS_2, $MoSe_2$, WS_2, and WSe_2 atomic layers, Nano Lett. **15**, 2526 (2015).
[35] J. Ribeiro-Soares, R. M. Almeida, E. B. Barros, P. T. Araujo, M. S. Dresselhaus, L. G. Cançado, and A. Jorio, Group theory analysis of phonons in two-dimensional transition metal dichalcogenides, Phys. Rev. B **90**, 115438 (2014).
[36] G. Kresse and J. Furthmüller, Efficient iterative schemes for *ab initio* total-energy calculations using a plane-wave basis set, Phys. Rev. B **54**, 11169 (1996).
[37] P. E. Blöchl, Projector augmented-wave method, Phys. Rev. B **50**, 17953 (1994).
[38] J. P. Perdew, K. Burke, and M. Ernzerhof, Generalized gradient approximation made simple, Phys. Rev. Lett. **77**, 3865 (1996).
[39] S. Grimme, J. Antony, S. Ehrlich, and H. Krieg, A consistent and accurate *ab initio* parametrization of density functional dispersion correction (DFT-D) for the 94 elements H-Pu, J. Chem. Phys. **132**, 154104 (2010).
[40] P. Yeh and M. Hendry, Optical waves in layered media, Phys. Today **43**, No. 1, 77 (1990).
[41] X.-L. Li, X.-F. Qiao, W.-P. Han, Y. Lu, Q.-H. Tan, X.-L. Liu, and P.-H. Tan, Layer number identification of intrinsic and defective multilayer graphenes by the Raman mode intensity from substrate, Nanoscale **7**, 8135 (2015).
[42] W. Zhao *et al.*, Evolution of electronic structure in atomically thin sheets of WS_2 and WSe_2, ACS Nano **7**, 791 (2012).
[43] Q.-H. Tan, Y.-J. Sun, X.-L. Liu, Y. Zhao, Q. Xiong, P.-H. Tan, and J. Zhang, Observation of forbidden phonons, Fano

resonance and dark excitons by resonance Raman scattering in few-layer WS_2, 2D Mater. **4**, 031007 (2017).

[44] D. Y. Qiu, F. H. da Jornada, and S. G. Louie, Optical spectrum of MoS_2: Many-body effects and diversity of exciton states, Phys. Rev. Lett. **111**, 216805 (2013).

[45] K. Takeyama, R. Moriya, S. Okazaki, Y. Zhang, S. Masubuchi, K. Watanabe, T. Taniguchi, T. Sasagawa, and T. Machida, Resonant tunneling due to van der Waals quantum-well states of few-layer WSe_2 in WSe_2/h-BN/p^+-MoS_2 junction, Nano Lett. **21**, 3929 (2021).

[46] M. Cazayous, J. Groenen, A. Zwick, A. Mlayah, R. Carles, J. L. Bischoff, and D. Dentel, Resonant Raman scattering by acoustic phonons in self-assembled quantum-dot multilayers: From a few layers to superlattices, Phys. Rev. B **66**, 195320 (2002).

[47] C. Jönsson, Electron diffraction at multiple slits, Am. J. Phys. **42**, 4 (1974).

[48] Miao-Ling Lin, https://www.researchgate.net/publication/388382276.